LETTER

CO₂ Reduction to CO with 19% Efficiency in a Solar-Driven Gas Diffusion Electrode Flow Cell under Outdoor Solar Illumination

Wen-Hui Cheng, Matthias H. Richter, Ian Sullivan, David M. Larson, Chengxiang Xiang, Bruce S. Brunschwig,* and Harry A. Atwater*

Read Online

ACCESS | Metrics & More | Article Recommendations | SI Supporting Information

ABSTRACT: Solar-driven reduction of carbon dioxide represents a carbon-neutral pathway for the synthesis of fuels and chemicals. We report here results for solar-driven CO_2 reduction using a gas diffusion electrode (GDE) directly powered by a photovoltaic cell. A GaInP/GaInAs/Ge triple-junction photovoltaic cell was used to power a *reverse-assembled* gas diffusion electrode employing a Ag nanoparticle catalyst layer. The device had a solar-to-CO energy conversion efficiency of 19.1% under simulated AM 1.5G illumination at 1 Sun. The use of a reverse-assembled GDE prevented transition from a wetted to a flooded catalyst bed and allowed the device to operate stably for >150 h with no loss in efficiency. Outdoor measurements were performed under ambient solar illumination in Pasadena, California, resulting in a peak solar-to-CO efficiency of 18.7% with a CO production rate of 47 mg·cm⁻² per day and a diurnal-averaged solar-to-fuel conversion efficiency of 5.8%.
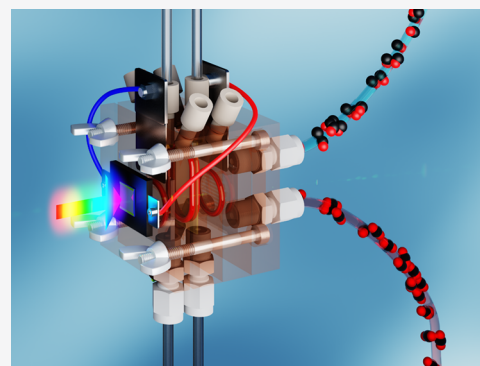
Solar photovoltaic and wind energy conversion are rapidly growing sources of low-carbon electric power.[1] However, the intermittency of solar and wind resources over wide time scales ranging from minutes to months means solar electricity is not a dispatchable power source. Thus, efficient and inexpensive approaches for energy storage are needed for wide penetration of renewable energy into the power grid.[2,3] While electrical energy storage in batteries may be important for short-term storage and grid power management, seasonal energy storage is unlikely to rely on batteries. Transformation of solar energy into chemical bonds provides a long-term energy storage strategy that opens a path for the synthesis of fuels and chemicals.[4] One approach to chemical energy storage is via solar-driven hydrogen generation, where (i) photovoltaics supply carbon-free electricity to the grid that is used to generate H_2 by water electrolysis at high current densities;[5] (ii) photovoltaics are used to directly drive electrolysis at low current densities,[6] or (iii) an integrated photoelectrochemical device performs unassisted direct water splitting to form H_2.[7,8] Parallel to solar hydrogen generation approaches, pathways for solar-driven reduction of carbon dioxide to fuels have used (i) direct electrolysis,[9] (ii) photovoltaic directly driven electrolysis,[10] and (iii) integrated photoelectrochemical conversion.[11,12] Of particular interest is solar-driven reduction of carbon dioxide using a high-efficiency photovoltaic (PV) device directly coupled to an electrochemical cell tailored for

reduction of CO_2 to CO.[13,14] Mixtures of solar-generated CO and H_2[15] could be used as syngas precursors in a future Fischer−Tropsch chemical synthesis process[16] to produce high molecular weight hydrocarbon fuels or chemicals as products.[17] Carbon dioxide reduction to CO is generally more energy efficient and kinetically easier than direct reduction of CO_2 to multicarbon products.[14,18,19]

Among the most efficient heterogeneous solid-state catalysts for CO_2 reduction to CO are gold,[20,21] silver,[22] WSe_2,[23] and MoS_2.[24] The use of high surface area morphology structures such as nanoparticles can improve catalytic activity.[25] Other factors that impact catalytic performance include catalyst morphology,[20] cations present in the electrolyte solution,[26] electrolyte concentration,[27] and local pH.[28] The state-of-the-art CO_2-to-CO conversion using a Au needle catalyst[27] showed an operating current of 15 mA·cm⁻² and 95% Faradaic efficiency at −0.35 V vs RHE. However, the current record efficiency device for solar conversion of CO_2 to CO using a solution-based electrochemical cell suffered from low current density (0.33 mA·cm⁻² at −0.6 V vs RHE) due to limited
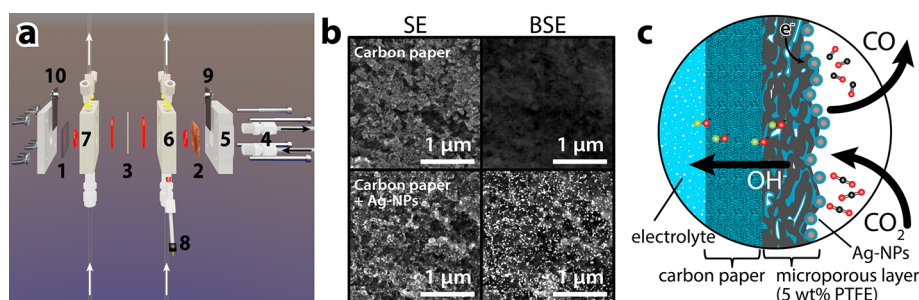
Figure 1. Gas diffusion electrode with Ag-NP catalyst. (a) Cell configuration composed of (1) NiO_x or Pt anode, (2) Ag-NPs on Sigracet 29BC carbon paper cathode, (3) anion exchange membrane, (4) CO_2 gas inlet and CO/CO_2 outlet, (5) acrylic backplate, (6) catholyte chamber, (7) anolyte chamber, (8) reference electrode, (9) GDE (cathode) power connector, and (10) anode power connector. Black arrows indicate the gas flow, and white arrows indicate the electrolyte flow. Note that the backplate (5) is designed to use an interdigitated wire electrode flow field to enhance the interaction between gas and catalysts and improve CO_2 utilization (see also Figure S1). (b) Scanning electron microscopy images of carbon paper without (top) and with (bottom) Ag-NP catalyst, secondary electrons image (left row) backscattered electrons image (right row). (c) Illustration of the reverse-assembled GDE cathode cross-section with wetted catalyst and operation for CO_2 reduction.

catalyst activity. This required the use of large-area electrodes to match the photovoltaic device area.[10] Table S1 shows overpotential and Faradaic efficiency data at current densities close to 15 mA·cm^{-2} along with the electrolyte conditions and catalyst loading for various Ag and Au electrodes. The catalytic activities shown in Table S1 indicate that in many cases nanoparticles of Ag have an activity similar to that of Au while costing significantly less.

Bulk aqueous electrolyte cells can exhibit high catalyst overpotentials due to the limited solubility of CO_2 (33.4 mM) in the electrolyte, a limited pH operating range of ~6−10, and slow ionic transport in the solution. In contrast, gas diffusion electrode (GDE) assemblies do not suffer these same restrictions.[29−35] In a GDE using 1 atm CO_2 vapor, CO_2 is transported in the vapor phase and reacts at a thin (<100 nm) solid−liquid−gas phase interface. In this configuration, liquid-state concentration and diffusion do not limit the conversion rate, resulting in lower overpotentials and higher current densities for CO_2 reduction.[30] Simulations have also shown that a cell using a thin (10 nm) layer of electrolyte on the catalysts (wetted catalyst) outperforms cells with either a completely dry or a completely flooded catalyst configuration.[36] These insights have led to the development of gas diffusion electrodes[37] and membrane electrode assemblies (MEA)[38] with a humidified gas supply to facilitate ion conduction and water balance.

Although membrane electrode assembly systems are more scalable, they often suffer from short-term stability due to salt precipitation or membrane dehydration at high current densities.[39] Hence, we chose to work with an aqueous GDE cell configuration. In this work, we employ a triple-junction photovoltaic (PV) device directly coupled with a gas diffusion electrode (GDE) as the first demonstration of an electrolyte flow type PV-GDE reactor that provides both high selectivity and long-term stability. For a directly driven PV-GDE system, the power generated by the PV is directly supplied to the GDE. In our device, the areas of the PV photoabsorber (A_{PV}) and GDE (A_{GDE}) were both 0.31 cm^2. To match the lower current density of the PV cell with the operating conditions of the anode, a relatively low catalyst loading of GDE was chosen. A Ag nanoparticle catalyst was used because of its relatively high activity and relatively low cost (Table S1).

Figure 1a is an illustration of the compression flow cell employed for the evaluation of gas diffusion electrode catalytic

performance. Dilute silver nanoparticles (Ag-NPs) with diameters of ≤50 nm were drop cast onto the microporous side of the GDE substrate (Sigracet 29BC). The loading of Ag-NPs in this work was measured to be 0.12 mg·cm^{-2}. A detailed description can be found in Methods in the Supporting Information. Scanning electron microscopy (SEM) images of the microporous layer with and without Ag-NPs are shown in Figure 1b. Gas was delivered to the GDE through an interdigitated electrode flow field (Figures 1a and S1) against which the GDE is compressed to maximize the interaction of CO_2 with the catalyst and gas utilization.[40] Current to the GDE was supplied through the interdigitated electrode to Ag-NP/carbon paper substrate. Gaseous products were collected at the outlet of the flow field, which was directly connected to a gas chromatograph (for more information see Methods in the Supporting Information).

An issue for aqueous GDEs is flooding or saturation of the porous catalyst layer with electrolyte or water during operation. This results in a thick (>1 μm) electrolyte layer and a diffusion-limited supply of CO_2 to the electrode.[41] To maintain the catalyst in a wetted but not flooded condition that minimizes losses of CO_2 to the electrolyte and extends the operational lifetime, we assembled our aqueous GDE in a nontraditional manner with the catalyst coating of Ag-NPs facing away from the electrolyte and toward the CO_2 gas supply. We denote this configuration as a *reverse-assembled* GDE. The microporous layer of the GDE was treated with polytetrafluoroethylene (PTFE), which helped to prevent flooding. Needle valves in the gas and liquid output streams allowed separation of the liquid and gas phases as well as control of the pressure difference between the aqueous electrolyte and the CO_2 stream. Contact angle analysis indicated that the Ag-NP coated surface was significantly less hydrophobic than the surface without Ag-NPs. Contact angle and optical microscope images of the GDE are shown in Figure S2.

With both the gas inlet and outlet on the same side of the GDE, the device operates in a "flow-by" GDE configuration. The Ag-NP catalyst side of the electrode was facing the CO_2 gas channel as illustrated in Figure 1c. This orientation of the Ag-NPs maintained a thin electrolyte layer on the catalyst and enhanced the rate of CO_2 reduction.[36] The turnover frequency of the Ag-NP catalyst for the reverse-assembled GDE at −0.6 V vs RHE was calculated as ~9 × 10^3 h^{-1} (see the Supporting
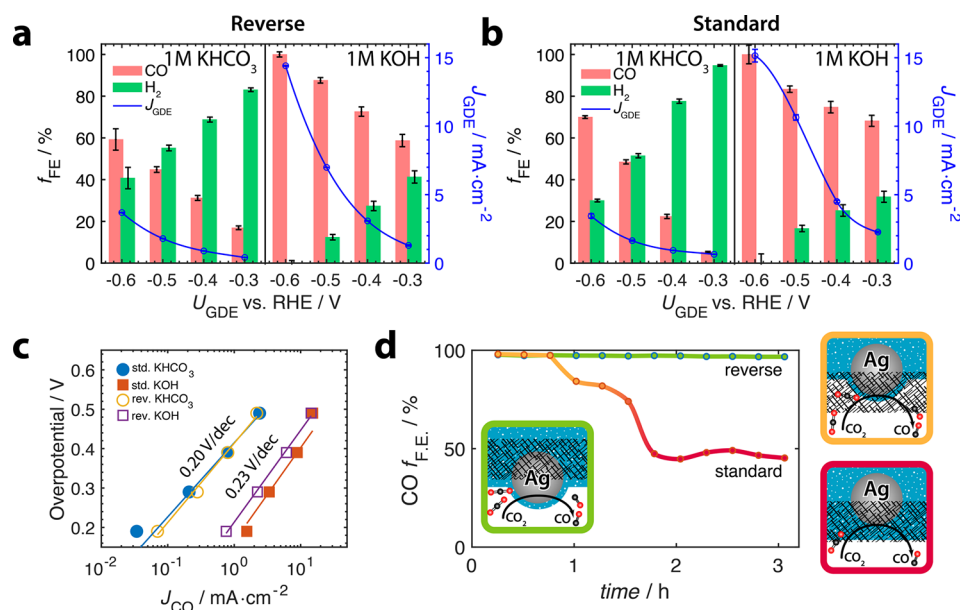
Figure 2. Dark catalysis three-electrode measurement of Ag-NPs GDE. Faradaic efficiency versus GDE potential operated in 1 M $KHCO_3$ (left half of graph) or 1 M KOH (right half of graph) of (a) the reserve-assembled Ag-NP GDE and (b) a standard-assembled Ag-NP GDE. (c) Overpotential versus CO partial current of Ag-NPs GDE for CO_2 reduction to CO. Overpotential = |$U_{GDE,RHE}$ + 0.11 V|, $J_{CO} \equiv J_{GDE} \times f_{FE,CO}$. (d) Stability of reserve-assembled and standard-assembled Ag-NPs GDE operated at −0.6 V vs RHE in 1 M KOH.

Information). The anode was made from either Pt or an electrochemically activated Ni foam for three- and two-electrode measurements, respectively. An aqueous catholyte of 1 M aqueous potassium bicarbonate ($KHCO_3$) or potassium hydroxide (KOH) was used under near neutral or basic conditions, respectively. In all cases, 1 M KOH was the anolyte. The anion exchange membrane (AEM) was Selemion for neutral environment or Fumasep FAA-3-50 for alkaline environment. Electrolyte (500 mL) was continuously pumped through the cathode chamber in a closed loop at a rate of 2 mL·min^{-1}. A change of pH (from 14 to 13.7) was observed for the 1 M KOH catholyte after 150 h of continuous operation, corresponding to irreversible loss of 0.25 mol KOH (50% of the electrolyte; see the Supporting Information). Further improvement to reduce CO_2 loss or regenerate the electrolyte would be necessary for fully sustainable operation. The neutralized carbonate electrolyte can possibly be utilized in a carbonate-to-syngas system to compensate the loss of CO_2 in a gas-fed MEA cell with a bipolar membrane.[42]

Results from three-electrode measurements for reverse- and standard-assembled GDEs are shown in panels a and b of Figure 2, respectively, for 1 M $KHCO_3$ (bulk pH of 8.5) and 1 M KOH (bulk pH of 14). Current densities are substantially lower than for earlier reported GDE devices because of the low catalyst loading used to match the current from the PV (current matching). For the reverse-assembled GDE, both the Faradaic efficiency ($f_{FE,CO}$) for CO and current density (J_{GDE}) increased with increasing potential with $f_{FE,CO}$ close to 100% at −0.6 V vs RHE in 1 M KOH (Figure 2a). Similar trends of current density and Faradaic efficiency versus applied potential were found for the standard-assembled GDE (Figure 2b). To compare the activity of the Ag-NPs in different orientations and pH, overpotential analysis for CO_2 reduction to CO was preformed (Figure 2c). The comparable Tafel slopes (~0.23 V/dec) in $KHCO_3$ and KOH for either orientation indicate a similar catalytic pathway regardless of the operating conditions. The Tafel behavior plotted with potentials vs NHE falls on a

rough single line (Figure S3) and suggests that the rate-determining step for the reduction on our Ag-NP GDE is not proton-limited. The achievable current density and Faradaic efficiency ($f_{FE,CO}$) for CO are higher in 1 M KOH than in 1 M $KHCO_3$ at the same overpotential (Figure 2c), likely because of a pH-independent rate-determining step. All subsequent measurements were, therefore, performed using 1 M KOH for the PV-GDE integrated device.

Figure 2d shows the Faradaic efficiency for CO versus time at −0.6 V vs RHE for the two GDE orientations in KOH. For the standard configuration, the $f_{FE,CO}$ decreased to ~75% after 1 h and to 50% after 2 h, while for the reverse configuration, the $f_{FE,CO}$ was ~97% for 3 h. Though similar in initial current density and $f_{FE,CO}$, the standard assembly, with the Ag-NP catalyst facing the electrolyte, became flooded during the first hour of operation resulting in a reduction of the Faradaic efficiency.

We performed two-electrode measurements for the GDE using an electrochemically activated nickel foam anode coupled to the GaInP/GaInAs/Ge triple-junction cell. For detailed information about the solar cell see Methods Figures S4 and S5, and Table S2 in the Supporting Information. A schematic of the cell is shown in Figure 3a with 1 M KOH as electrolyte using a Fumasep FAA-3-50 membrane. Both the cell potential (U_{cell}) and the cathode-to-reference electrode potential (U_{GDE}) were monitored during the operation. We calculated the solar-to-fuel efficiency (η_{STF}) for CO_2 reduction using eq 1.

$$\eta_{STF} = \frac{P_{out}}{P_{in}} = \frac{J_{GDE} \cdot \Delta U_{rxn} \cdot f_{FE,CO} \cdot A_{GDE}}{P_{light} \cdot A_{PV}} = \frac{J \cdot \Delta U_{rxn} \cdot f_{FE,CO}}{P_{light}}$$

(1)

where ΔU_{rxn} is the thermodynamic potential difference between the oxygen evolution half reaction (OER) and the CO_2 reduction half reaction of 1.34 V, A the area of the GDE or PV with $A_{GDE} = A_{PV} = 0.31$ cm^2, J (= $J_{GDE} = J_{PV}$) the
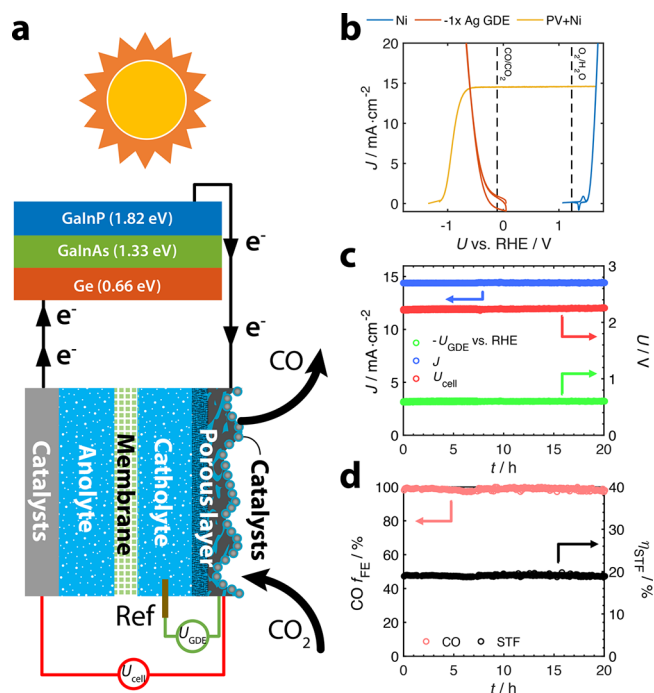
Figure 3. Light driven PV-GDE measurement ($A_{PV} = A_{GDE} = 0.31$ cm^2). (a) Illustration of wire connection between the triple-junction cell and GDE cell. (b) $J-U$ characteristic of Ni anode, solar cell with Ni anode, and Ag-NP gas diffusion cathode under 1 Sun. (c) Current, GDE potential vs RHE, and cell voltage measurement over 20 h duration. (d) Corresponding CO Faradaic efficiency and solar-to-fuel efficiency over the same 20 h duration.

operation current density of the system, and P_{light} the incident light irradiance (mW·cm^{-2}) on the photovoltaic cell. The energy efficiency for the GDE cell (η_{GDE}) was defined as follows:

$$\eta_{GDE} = \frac{P_{out}}{P_{in}} = \frac{\Delta U_{rxn} \cdot J_{GDE} \cdot A_{GDE} \cdot f_{FE,CO}}{U_{cell} \cdot J_{PV} \cdot A_{PV}} = \frac{\Delta U_{rxn} \cdot f_{FE,CO}}{U_{cell}} \tag{2}$$

where $J_{GDE} \cdot A_{GDE} = J_{PV} \cdot A_{PV}$ and U_{cell} is the total operating voltage of the cell.

To evaluate the efficiency and stability, we measured cell parameters using simulated AM 1.5G sun illumination at 1 Sun in the laboratory, as shown in Figure 3b–d. The blue curve in Figure 3b represents the performance of the electrochemically activated Ni foam anode alone, while the yellow curve indicates the behavior of PV plus anode. The red curve shows the catalytic current of the Ag-NPs GDE. The intersection between the red and yellow curves in Figure 3b defines the operation point, located at −0.6 V vs RHE and 14.4 mA·cm^{-2} with a cell voltage of 2.23 V. Panels c and d of Figure 3 illustrate the cell performance over 20 h with an average Faradaic efficiency for CO of 99 ± 2% and an average CO production rate of 2.3 mg·h^{-1}. No degradation in performance was observed. From the experimental results, we calculated the average solar-to-CO efficiency for the 20 h operation as 19.1 ± 0.2%, with an average energy efficiency η_{GDE} of 59.4 ± 0.6%. The error bars were obtained as the variation within the 20 h of operation. All the experimental results are summarized in Table S3. The chemical composition of the Ag-NP catalyst layer was examined before and after the reaction by X-ray photoelectron spectroscopy as shown in Figure S6. No obvious

changes were observed other than the absorption of potassium after operation with the Ag-NP catalyst maintaining its metallic phase.

The solar-to-CO efficiency of 19.1% represents a new record efficiency. A performance comparison with the current state-of-the-art PV-electrolyzer for CO_2 reduction to CO is shown in Table S4. The PV-GDE device had a CO production rate per projected cathode area 50 times higher than for the bulk electrolyte device (7.4 mg·h^{-1}·cm^{-2} versus 0.145 mg·h^{-1}·cm^{-2}) with greatly improved stability (20 h with no degradation versus 15% loss in 5 h).[10] A similar PV-GDE device operated under 3.25 Suns illumination with $A_{GDE} = 1$ cm^2 and $A_{PV} = 0.31$ cm^2 ($3.25 \approx A_{GDE}/A_{PV}$) showed over 150 h of stability, with an average Faradaic efficiency of 96 ± 2%, an average solar-to-CO efficiency of 18.9 ± 0.5%, and an average energy efficiency η_{GDE} of 53.7 ± 1.2% (Figure S7).

Full day outdoor tests were conducted with online gas product analysis in order to obtain the solar-to-fuel efficiency over the entire day. Results are shown in Figure 4. The triple-
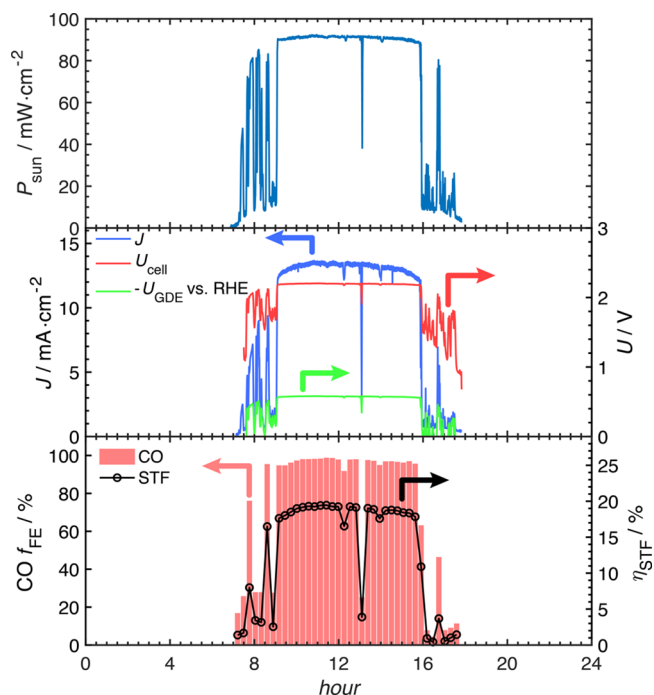

Figure 4. Outdoor assessments of solar-driven PV-GDE in Pasadena, CA ($A_{PV} = A_{GDE} = 0.31$ cm^2). The solar irradiance was monitored with a calibrated silicon photodiode. Operating current density J ($= J_{GDE} = J_{PV}$), cell voltage U_{cell}, GDE potential U_{GDE} vs RHE, CO Faradaic efficiency $f_{FE,CO}$, and solar-to-fuel efficiency η_{STF} were recorded for a 24 h day cycle.

junction cell and a calibrated silicon photodiode were mounted on a solar tracker to maintain optimum orientation toward the Sun (see illustration in Figure S8). The dips in sun intensity at 7:00–9:00 a.m. and 4:00–6:00 p.m. in the data were the result of trees blocking the sunlight. The system operated at a cell voltage of 2.20 V and GDE potential of −0.57 V vs RHE under natural full sun illumination. A Faradaic efficiency of 96 ± 8% and solar-to-fuel conversion efficiency of 18.7 ± 1.7% was observed over an optimal 6 h period within the day. The diurnal-averaged solar-to-fuel conversion efficiency was 5.8%. The CO production rate for 1 day under actual outdoor sun conditions was calculated to be 15 mg·day^{-1} of CO. Another

outdoor demonstration used a lens to concentrate the sunlight, producing an irradiance of 3.25 Suns ($C = 3.25$, $A_{GDE} = 1$ cm^2, $A_{PV} = 0.31$ cm^2) with data included in Figure S9 and Table S3 with a CO generation rate of 50 mg·day^{-1}. Using this calculated rate, a system scale up to 1 m^2 would result in a CO production rate of 0.5 kg·day^{-1}.

The performance of our directly coupled PV-GDE device was compared to a DC–DC converter coupled PV and GDE with power-matching electronics. We simulate DC–DC converter output curves with the input of our solid-state PV curve as shown in Figure S10. Though the DC–DC converter can track the maximum power point (MPP) of the PV, a practical loss of 5–10% is expected.[43] The operating point for the directly driven PV-GDE cell is $U_{cell} = 2.23$ V and $J = 14.4$ mA·cm^{-2} with a maximum efficiency of 19.3%. With a 95% efficient DC–DC converter, the operation point would be $U_{cell} = 2.22$ V and $J = 13.8$ mA·cm^{-2} with a maximum efficiency of 18.5%. For a 90% efficient DC–DC converter, the operation point would be $U_{cell} = 2.20$ V and $J = 13.2$ mA·cm^{-2} with a maximum efficiency of 17.7%. The maximum efficiencies are calculated assuming 100% CO Faradaic efficiency. All systems are summarized in Table S3. The slightly higher efficiency of our directly driven PV-GDE device, compared to the same setup with integrated DC–DC converter and power matching electronics, reveals the potential of developing a directly coupled PV-GDE device with its reduced complexity.

In summary, we have demonstrated a highly efficient solar-driven CO$_2$ reduction device for CO generation using a flow-by reverse-assembled gas diffusion electrode cell directly coupled to a triple-junction solar cell. The reverse-assembled GDE is designed to minimize parasitic CO$_2$ losses, utilizing a high CO$_2$ concentration and low overpotential catalysts for the CO$_2$ reduction reaction. The Ag-NPs-based catalyst exhibited near unity Faradaic efficiency toward CO generation at approximately −0.6 V vs RHE in 1 M KOH electrolyte. The PV-GDE system was evaluated under both laboratory AM 1.5G simulated solar irradiation and outdoor real sun conditions. Near-unity Faradaic efficiency was observed for CO$_2$-to-CO conversion, and an average solar-to-CO energy efficiency of 19.1% was achieved with AM 1.5G illumination at 1 Sun, leading to a CO production rate per catalyst area over 50 times higher than that of the current record photovoltaic-driven electrolysis device. The GDE was demonstrated to be stable for over 150 h without degradation, supporting our hypothesis that, by using a reverse-assembled GDE device configuration with the catalyst layer facing toward the CO$_2$ gas supply, we could extend the system operation time without suffering a transition from a wetted to a flooded gas diffusion layer. Under outdoor sun conditions, the PV-GDE system exhibited a solar-to-CO conversion efficiency of 18.7% during noontime and yielded a CO production rate of 15 mg·cm^{-2} per day. This reverse-assembled PV-GDE establishes a new efficiency record for directly solar-driven CO$_2$ reduction and offers an example of a very high-efficiency, stable device for solar CO$_2$ conversion.

ASSOCIATED CONTENT

Ⓢ Supporting Information

The Supporting Information is available free of charge at https://pubs.acs.org/doi/10.1021/acsenergylett.9b02576.

Methods, calculations of solar-to-fuel efficiency, GDE efficiency, turnover frequency, cell potentials, CO$_2$ loss, and supporting figures and tables (PDF)

■ AUTHOR INFORMATION

Corresponding Authors

Bruce S. Brunschwig − *California Institute of Technology, Pasadena, California*; Email: bsb@caltech.edu

Harry A. Atwater − *California Institute of Technology, Pasadena, California*; Ⓞ orcid.org/0000-0001-9435-0201; Email: haa@caltech.edu

Other Authors

Wen-Hui Cheng − *California Institute of Technology, Pasadena, California*; Ⓞ orcid.org/0000-0003-3233-4606

Matthias H. Richter − *California Institute of Technology, Pasadena, California*; Ⓞ orcid.org/0000-0003-0091-2045

Ian Sullivan − *California Institute of Technology, Pasadena, California*; Ⓞ orcid.org/0000-0003-0632-4607

David M. Larson − *Lawrence Berkeley National Laboratory,, Berkeley, California*

Chengxiang Xiang − *California Institute of Technology, Pasadena, California*; Ⓞ orcid.org/0000-0002-1698-6754

Complete contact information is available at:
https://pubs.acs.org/10.1021/acsenergylett.9b02576

Author Contributions

W.-H.C., M.H.R., and H.A.A. conceived of the experimental study. W.-H.C. and M.H.R. executed the experiments and did the data analysis. D.M.L., I.S., B.S.B., and C.X. provided technical support and scientific discussion. W.-H.C., M.H.R., B.S.B., and H.A.A. wrote the Letter, and all authors commented on the manuscript.

Notes

The authors declare no competing financial interest.

■ REFERENCES

(1) Davis, S. J.; Lewis, N. S.; Shaner, M. R.; Aggarwal, S.; Arent, D.; Azevedo, I. L.; Benson, S. M.; Bradley, T.; Brouwer, J.; Chiang, Y.-M.; Clack, C. T. M.; Cohen, A.; Doig, S.; Edmonds, J.; Fennell, P.; Field, C. B.; Hannegan, B.; Hodge, B.-M.; Hoffert, M. I.; Ingersoll, E.; Jaramillo, P.; Lackner, K. S.; Mach, K. J.; Mastrandrea, M.; Ogden, J.; Peterson, P. F.; Sanchez, D. L.; Sperling, D.; Stagner, J.; Trancik, J. E.; Yang, C.-J.; Caldeira, K. Net-Zero Emissions Energy Systems. *Science* **2018**, *360* (6396), No. eaas9793.

(2) Armstrong, R. C.; Wolfram, C.; de Jong, K. P.; Gross, R.; Lewis, N. S.; Boardman, B.; Ragauskas, A. J.; Ehrhardt-Martinez, K.; Crabtree, G.; Ramana, M. V. The Frontiers of Energy. *Nature Energy* **2016**, *1* (1), 15020.

(3) Shaner, M. R.; Davis, S. J.; Lewis, N. S.; Caldeira, K. Geophysical Constraints on the Reliability of Solar and Wind Power in the United States. *Energy Environ. Sci.* **2018**, *11* (4), 914−925.

(4) Lewis, N. S. Toward Cost-Effective Solar Energy Use. *Science* **2007**, *315* (5813), 798−801.

(5) Gray, E. M.; Webb, C. J.; Andrews, J.; Shabani, B.; Tsai, P. J.; Chan, S. L. I. Hydrogen Storage for Off-Grid Power Supply. *Int. J. Hydrogen Energy* **2011**, *36* (1), 654−663.

(6) Jia, J.; Seitz, L. C.; Benck, J. D.; Huo, Y.; Chen, Y.; Ng, J. W. D.; Bilir, T.; Harris, J. S.; Jaramillo, T. F. Solar Water Splitting by Photovoltaic-Electrolysis with a Solar-to-Hydrogen Efficiency Over 30%. *Nat. Commun.* **2016**, *7*, 13237.

(7) Young, J. L.; Steiner, M. A.; Döscher, H.; France, R. M.; Turner, J. A.; Deutsch, T. G. Direct Solar-to-Hydrogen Conversion via Inverted Metamorphic Multi-Junction Semiconductor Architectures. *Nature Energy* **2017**, *2*, 17028.

(8) Cheng, W.-H.; Richter, M. H.; May, M. M.; Ohlmann, J.; Lackner, D.; Dimroth, F.; Hannappel, T.; Atwater, H. A.; Lewerenz, H. J. Monolithic Photoelectrochemical Device for Direct Water Splitting with 19% Efficiency. *ACS Energy Lett.* **2018**, *3* (8), 1795−1800.

(9) Seh, Z. W.; Kibsgaard, J.; Dickens, C. F.; Chorkendorff, I.; Nørskov, J. K.; Jaramillo, T. F. Combining Theory and Experiment in Electrocatalysis: Insights Into Materials Design. *Science* **2017**, *355* (6321), No. eaad4998.

(10) Schreier, M.; Héroguel, F.; Steier, L.; Ahmad, S.; Luterbacher, J. S.; Mayer, M. T.; Luo, J.; Grätzel, M. Solar Conversion of CO_2 To CO Using Earth-Abundant Electrocatalysts Prepared by Atomic Layer Modification of CuO. *Nature Energy* **2017**, *2* (7), 17087.

(11) Gurudayal; Beeman, J. W.; Bullock, J.; Wang, H.; Eichhorn, J.; Towle, C.; Javey, A.; Toma, F. M.; Mathews, N.; Ager, J. W., III Si Photocathode with Ag-Supported Dendritic Cu Catalyst for CO_2 Reduction. *Energy Environ. Sci.* **2019**, *12* (3), 1068−1077.

(12) Zhou, X.; Liu, R.; Sun, K.; Chen, Y.; Verlage, E.; Francis, S. A.; Lewis, N. S.; Xiang, C. Solar-Driven Reduction of 1 atm of CO_2 To Formate at 10% Energy-Conversion Efficiency by Use of a TiO_2-Protected III−V Tandem Photoanode in Conjunction with a Bipolar Membrane and a Pd/C Cathode. *ACS Energy Lett.* **2016**, *1* (4), 764−770.

(13) Romero Cuellar, N. S.; Wiesner-Fleischer, K.; Fleischer, M.; Rucki, A.; Hinrichsen, O. Advantages of CO Over CO_2 As Reactant for Electrochemical Reduction to Ethylene, Ethanol and N-Propanol on Gas Diffusion Electrodes at High Current Densities. *Electrochim. Acta* **2019**, *307*, 164−175.

(14) Zhou, X.; Xiang, C. Comparative Analysis of Solar-to-Fuel Conversion Efficiency: a Direct, One-Step Electrochemical CO_2 Reduction Reactor Versus a Two-Step, Cascade Electrochemical CO_2 Reduction Reactor. *ACS Energy Lett.* **2018**, *3* (8), 1892−1897.

(15) Delacourt, C.; Ridgway, P. L.; Kerr, J. B.; Newman, J. Design of an Electrochemical Cell Making Syngas ($CO + H_2$) From CO_2 And H_2O Reduction at Room Temperature. *J. Electrochem. Soc.* **2008**, *155* (1), B42−B49.

(16) Schulz, H. Short History and Present Trends of Fischer−Tropsch Synthesis. *Appl. Catal., A* **1999**, *186* (1−2), 3−12.

(17) Nielsen, D. U.; Hu, X.-M.; Daasbjerg, K.; Skrydstrup, T. Chemically and Electrochemically Catalysed Conversion of CO_2 To CO with Follow-Up Utilization to Value-Added Chemicals. *Nature Catalysis* **2018**, *1* (4), 244−254.

(18) Lum, Y.; Ager, J. W., III. Sequential Catalysis Controls Selectivity in Electrochemical CO_2 Reduction on Cu. *Energy Environ. Sci.* **2018**, *11* (10), 2935−2944.

(19) Jouny, M.; Luc, W.; Jiao, F. High-Rate Electroreduction of Carbon Monoxide to Multi-Carbon Products. *Nature Catalysis* **2018**, *1* (10), 748−755.

(20) Welch, A. J.; DuChene, J. S.; Tagliabue, G.; Davoyan, A.; Cheng, W.-H.; Atwater, H. A. Nanoporous Gold as a Highly Selective and Active Carbon Dioxide Reduction Catalyst. *ACS Appl. Energy Mater.* **2019**, *2* (1), 164−170.

(21) Chen, Y.; Li, C. W.; Kanan, M. W. Aqueous CO_2 Reduction at Very Low Overpotential on Oxide-Derived Au Nanoparticles. *J. Am. Chem. Soc.* **2012**, *134* (49), 19969−19972.

(22) Hatsukade, T.; Kuhl, K. P.; Cave, E. R.; Abram, D. N.; Jaramillo, T. F. Insights Into the Electrocatalytic Reduction of CO_2 On Metallic Silver Surfaces. *Phys. Chem. Chem. Phys.* **2014**, *16* (27), 13814−13819.

(23) Asadi, M.; Kim, K.; Liu, C.; Addepalli, A. V.; Abbasi, P.; Yasaei, P.; Phillips, P.; Behranginia, A.; Cerrato, J. M.; Haasch, R.; Zapol, P.; Kumar, B.; Klie, R. F.; Abiade, J.; Curtiss, L. A.; Salehi-Khojin, A. Nanostructured Transition Metal Dichalcogenide Electrocatalysts for CO_2 Reduction in Ionic Liquid. *Science* **2016**, *353* (6298), 467−470.

(24) Asadi, M.; Kumar, B.; Behranginia, A.; Rosen, B. A.; Baskin, A.; Repnin, N.; Pisasale, D.; Phillips, P.; Zhu, W.; Haasch, R.; Klie, R. F.; Král, P.; Abiade, J.; Salehi-Khojin, A. Robust Carbon Dioxide Reduction on Molybdenum Disulphide Edges. *Nat. Commun.* **2014**, *5*, 4470.

(25) Cheng, T.; Huang, Y.; Xiao, H.; Goddard, W. A. Predicted Structures of the Active Sites Responsible for the Improved Reduction of Carbon Dioxide by Gold Nanoparticles. *J. Phys. Chem. Lett.* **2017**, *8* (14), 3317−3320.

(26) Singh, M. R.; Kwon, Y.; Lum, Y.; Ager, J. W., III; Bell, A. T. Hydrolysis of Electrolyte Cations Enhances the Electrochemical Reduction of CO_2 Over Ag and Cu. *J. Am. Chem. Soc.* **2016**, *138* (39), 13006−13012.

(27) Liu, M.; Pang, Y.; Zhang, B.; De Luna, P.; Voznyy, O.; Xu, J.; Zheng, X.; Dinh, C. T.; Fan, F.; Cao, C.; de Arquer, F. P. G.; Safaei, T. S.; Mepham, A.; Klinkova, A.; Kumacheva, E.; Filleter, T.; Sinton, D.; Kelley, S. O.; Sargent, E. H. Enhanced Electrocatalytic CO_2 Reduction via Field-Induced Reagent Concentration. *Nature* **2016**, *537* (7620), 382−386.

(28) Varela, A. S.; Kroschel, M.; Reier, T.; Strasser, P. Controlling the Selectivity of CO_2 Electroreduction on Copper: the Effect of the Electrolyte Concentration and the Importance of the Local pH. *Catal. Today* **2016**, *260*, 8−13.

(29) Verma, S.; Lu, X.; Ma, S.; Masel, R. I.; Kenis, P. J. A. The Effect of Electrolyte Composition on the Electroreduction of CO_2 To CO on Ag Based Gas Diffusion Electrodes. *Phys. Chem. Chem. Phys.* **2016**, *18* (10), 7075−7084.

(30) Higgins, D.; Hahn, C.; Xiang, C.; Jaramillo, T. F.; Weber, A. Z. Gas-Diffusion Electrodes for Carbon Dioxide Reduction: a New Paradigm. *ACS Energy Lett.* **2019**, *4* (1), 317−324.

(31) Singh, M. R.; Papadantonakis, K.; Xiang, C.; Lewis, N. S. An Electrochemical Engineering Assessment of the Operational Conditions and Constraints for Solar-Driven Water-Splitting Systems at Near-Neutral pH. *Energy Environ. Sci.* **2015**, *8* (9), 2760−2767.

(32) Lobaccaro, P.; Singh, M. R.; Clark, E. L.; Kwon, Y.; Bell, A. T.; Ager, J. W., III. Effects of Temperature and Gas−Liquid Mass Transfer on the Operation of Small Electrochemical Cells for the Quantitative Evaluation of CO_2 Reduction Electrocatalysts. *Phys. Chem. Chem. Phys.* **2016**, *18* (38), 26777−26785.

(33) Weng, L.-C.; Bell, A. T.; Weber, A. Z. Towards Membrane-Electrode Assembly Systems for CO_2 Reduction: a Modeling Study. *Energy Environ. Sci.* **2019**, *12* (6), 1950−1968.

(34) Song, J. T.; Song, H.; Kim, B.; Oh, J. Towards Higher Rate Electrochemical CO_2 Conversion: From Liquid-Phase to Gas-Phase Systems. *Catalysts* **2019**, *9* (3), 224.

(35) Li, J.; Chen, G.; Zhu, Y.; Liang, Z.; Pei, A.; Wu, C.-L.; Wang, H.; Lee, H. R.; Liu, K.; Chu, S.; Cui, Y. Efficient Electrocatalytic CO_2 Reduction on a Three-Phase Interface. *Nature Catalysis* **2018**, *1* (8), 592−600.

(36) Weng, L.-C.; Bell, A. T.; Weber, A. Z. Modeling Gas-Diffusion Electrodes for CO_2 Reduction. *Phys. Chem. Chem. Phys.* **2018**, *20*, 16973−16984.

(37) Cook, R. L.; MacDuff, R. C.; Sammells, A. F. High Rate Gas Phase CO_2 Reduction to Ethylene and Methane Using Gas Diffusion Electrodes. *J. Electrochem. Soc.* **1990**, *137* (2), 607−608.

(38) Hori, Y.; Ito, H.; Okano, K.; Nagasu, K.; Sato, S. Silver-Coated Ion Exchange Membrane Electrode Applied to Electrochemical Reduction of Carbon Dioxide. *Electrochim. Acta* **2003**, *48* (18), 2651−2657.

(39) *CRC Handbook of Chemistry and Physics*; Lide, D. R., Ed.; New York, 2003.

(40) Ripatti, D. S.; Veltman, T. R.; Kanan, M. W. Carbon Monoxide Gas Diffusion Electrolysis That Produces Concentrated C_2 Products with High Single-Pass Conversion. *Joule* **2019**, *3* (1), 240−256.

(41) Dinh, C. T.; Burdyny, T.; Kibria, M. G.; Seifitokaldani, A.; Gabardo, C. M.; de Arquer, F. P. G.; Kiani, A.; Edwards, J. P.; De Luna, P.; Bushuyev, O. S.; Zou, C.; Quintero-Bermudez, R.; Pang, Y.; Sinton, D.; Sargent, E. H. CO_2 Electroreduction to Ethylene via Hydroxide-Mediated Copper Catalysis at an Abrupt Interface. *Science* **2018**, *360* (6390), 783−787.

(42) Li, Y. C.; Lee, G.; Yuan, T.; Wang, Y.; Nam, D.-H.; Wang, Z.; Garcia de Arquer, F. P.; Lum, Y.; Dinh, C. T.; Voznyy, O.; Sargent, E. H. Co_2 Electroreduction From Carbonate Electrolyte. *ACS Energy Lett.* **2019**, *4* (6), 1427−1431.

(43) Hossain, M. Z.; Rahim, N. A.; Selvaraj, J. A. L. Recent Progress and Development on Power DC-DC Converter Topology, Control, Design and Applications: a Review. *Renewable Sustainable Energy Rev.* **2018**, *81*, 205−230.